Chapter 4

Serial Diffusion MRI to Monitor and Model Early Treatment Response to the Targeted Nanotherapy CRLX101

4.1 Abstract

4.1.1 Purpose

Targeted cancer nanotherapies are being developed to enhance local tumor therapeutic response. The nanotherapy CRLX101 (formerly IT-101), has been shown to be effective in preclinical models and is currently in clinical trials. We evaluated the efficacy of diffusion-weighted magnetic resonance imaging (diffusion MRI) to monitor early response of CRLX101 and to evaluate its potential as a therapeutic response predictor using a mechanistic model of tumor cell proliferation.

4.1.2 Experimental design

Diffusion MRI was serially performed following CRLX101 administration in a murine lymphoma model. Apparent diffusion coefficients (ADC) were extracted from the data and used as a treatment response biomarker. Animals treated with irinotecan (CPT-11) and saline were imaged for comparison. ADC data were input into a mathematical model of tumor growth to evaluate its ability

This section is being prepared for publication: Thomas S.C. Ng, David Wert, Hargun Sohi, Daniel Procissi, David Colcher, Andrew A. Raubitschek, Russell E. Jacobs. (2012) Serial diffusion MRI to monitor and model early treatment response to the targeted nanotherapy CRLX101.

Acknowledgments: We thank Dr. Thomas Schluep of Calando Pharmaceuticals for providing the CRLX101 (formerly IT-101), Dr. Andrey Demyanenko, Desiree Crow, Bita Alaghebandan, and Sonia Collazo for their technical assistance. Drs. Mark Davis, Yun Yen and Scott Fraser gave helpful advice and support. The project was funded by NIBIB R01 EB000993, NIH R01 EB00194, NRSA T32GM07616, City of Hope Lymphoma SPORE Grant (P50 CA107399), the Beckman Institute and the Caltech/City of Hope Biomedical Initiative.

to predict therapeutic response. Histological analysis using cleaved-caspase 3, TUNEL, Ki-67 and H&E were conducted on tumor samples for correlation with imaging results.

4.1.3 Results

Mean ADC changes for CRLX101 treated tumors at day 2, 4 and 7 post-treatment were 16 ± 9%, 24 ± 10% and 49 ± 17% respectively, which were statistically greater than the controls ($p \leq 0.02$) and noticeably greater than CPT-11 treated tumors (5 ± 5%, 14 ± 7% and 18 ± 6%). Model-derived parameters for cell proliferation obtained using ADC data distinguished CRLX101 treated tumors from controls.

4.1.4 Conclusions

Temporal changes in the functional imaging biomarker, ADC, specified early CRLX101 treatment response and could be used to model image-derived cell proliferation rates following treatment. Comparisons of different treatments (targeted and non-targeted) highlight the utility of noninvasive imaging and modeling to evaluate, monitor and predict responses to targeted nanotherapeutics.

4.2 Translational Relevance

Targeted nanotherapies are being developed for cancer treatment. The advantage of these therapies over conventional treatments lies in their ability to increase drug uptake in tumors while reducing treatment-related toxicity. The availability of clinically applicable biomarkers will facilitate the clinical translation of nanotherapies. We evaluated the applicability of diffusion MRI to monitor CRLX101 (a cyclodextrin-based polymer particle containing the DNA topoisomerase I inhibitor camptothecin) efficacy in a preclinical model of malignant lymphoma. Diffusion MRI distinguished animals treated with CRLX101 from controls as early as day 2 after treatment. Diffusion MRI also demonstrated the reduced efficacy of irinotecan compared to CRLX101. Incorporating diffusion MRI data into a mathematical model of tumor growth allowed prediction of the enhanced antiproliferative effect of CRLX101 as compared to the non-targeted agent. These results demonstrate that serial imaging using diffusion MRI, combined with judicious modeling of imaging data, provides useful biomarkers to evaluate, monitor and predict the efficacy of targeted nanotherapies in

the clinic.

4.3 Introduction

Targeted cancer nanotherapies are increasingly being explored as alternatives to conventional therapeutics. They have the potential to increase treatment efficacy and reduce treatment-related toxicity (TRT) through improved tumor drug delivery [22]. Compared to conventional therapies, nanoscale therapeutics show increased plasma half-life and can localize to the tumor mass via targeting mechanisms such as enhanced permeability and retention (EPR) [21, 214]. Recently, the EPR effect has been coupled with surface functionalization of particles [31] to improve retention in the tumor and target specific tumor cell subsets. Moreover, evidence exists that nanotherapies can also escape multidrug resistance pathways since their mode of cellular uptake can bypass P-glycoprotein efflux pumps that cause resistance to conventional drugs [214].

Nanotherapies may prove to be useful for the treatment of malignant lymphoma. Despite great advances in lymphoma management, over half of the patient population diagnosed with aggressive non-Hodgkin lymphoma, 30%–40% with advanced Hodgkin's lymphoma, and many with indolent lymphoma still develop resistance or relapse of the disease [215, 216, 217]. Several strategies, including the single or combined application of multi-drug chemotherapy, immunotherapy and radiation-based therapies, are currently being explored as salvage regimens [216, 217]. Important considerations during the treatment selection process include the need to minimize TRT to the patient as well as the need to avoid cross-resistance from first-line regimens [218, 217]. Thus, the use of targeted nanotherapies offers an interesting therapeutic alternative.

The nanoparticle CRLX101 (formerly IT-101, Cerulean Pharma Inc.) is a conjugate of a β–cyclodextrin-based polymer and 20(S)-campthothecin (CPT). CPT is a topoisomerase I inhibitor with a broad activity spectrum. CRLX101 increases the solubility of CPT, keeps CPT in its active lactone form, improves CPT tumor localization and minimizes CPT-associated TRT [24, 19]. Preclinical *in vivo* studies of CRLX101 demonstrated its efficacy in a broad range of solid tumors [217, 17], including subcutaneous and disseminated xenograft lymphoma models [217]. CRLX101 is currently in phase I and phase II trials for a variety of solid tumors [219].

A major challenge for clinical translation of cancer nanotherapies is the effective evaluation of

treatment response. Imaging technologies have been used to monitor responses to conventional therapy [220]. Typical methods rely on changes in tumor size [11, 221]. Morphological imaging using computerized tomography (CT), ultrasound and anatomical magnetic resonance imaging (MRI) can assess changes in the appearance or growth of tumor masses. However, such changes often occur at least several weeks after treatment, which may delay useful modifications of the treatment course. A functional imaging technique, diffusion MRI [222], is being investigated to evaluate therapeutic responses in animal models [223, 224] and human clinical studies [156, 225]. A quantitative metric derived from these studies, the apparent diffusion coefficient (ADC), has been shown to be sensitive to tumor therapy response. Although the diffusion of water within tumors is mediated by many complex processes, ADC has been demonstrated to be related to tumor cellularity and extracellular volume [226]. Increased ADC values over the course of a treatment time course are correlated with tumor treatment response to small molecule chemotherapy [223, 224], adoptive immunotherapy [227] and photodynamic therapy [33].

Mathematical models of cancer growth have been shown to predict tumor treatment response on an individual basis. Modeling adds an extra dimension to clinical management by enabling prospective, patient-specific adjustments of treatment regimens [228, 229]. noninvasive imaging data have been applied successfully to models of tumor growth and treatment response in brain [230, 132, 231, 232] and kidney [233] tumors. These studies demonstrate that incorporation of imaging data into mathematical models of tumor growth can provide insights at the cellular scale that may elude conventional measures of tumor progression, such as the RECIST criteria [234]. Furthermore, since the efficacy of nanotherapies is a complex function of the drug payload and the carrier's interaction with the tumor microenvironment [124], image-based modeling of treatment response may also provide mechanistic insights into the functioning of nanotherapies *in vivo*.

The purpose of this study is to determine the feasibility of diffusion MRI to evaluate and predict early treatment efficacy of the nanotherapy CRLX101. Using a preclinical model of Burkitt's lymphoma, we compared the diffusion MRI response of low dose CRLX101 to a high dose administration of a water-soluble CPT analog, irinotecan (CPT-11), and to controls. Further, serial diffusion MRI data were incorporated into a mathematical model of tumor cell proliferation to evaluate its ability to highlight and predict the antiproliferative activity of CRLX101 *in vivo*.

4.4 Materials and Methods

4.4.1 Cell Culture, Animal Model, and Human Lymphoma Xenograft Models

Daudi cells (human Burkitt's lymphoma line) were obtained from the American Type Culture Collection. Cells were maintained in sterile culture media as previously described [235]. Six to eight week old female athymic nu/nu mice (Charles River) were injected with 0.2 mL of 1:1: mixture of tumor cell suspension in 1% human serum albumin in HBSS (Mediatech) and Matrigel (BD Biosciences) subcutaneously into their right groin region. Approximately 3×10^6 cells were injected for each mouse. Mouse care and experimental procedures were carried out in accordance with protocols approved by the Research Animal Care Committee at the City of Hope and the Animal Care and Use Committee at Caltech.

4.4.2 *In Vivo* MRI Studies

A Biospec (Bruker-Biospin Inc. Billerica, MA) 7 T MRI scanner and a home-built birdcage coil with an 8 cm axial field of view (FOV) were used for mouse MRI image acquisition. For all imaging sessions, animals were anesthetized using 1.3%–1.75% isoflurane and body temperature was maintained at 36°C–37°C with warmed air flowing through the bore. For anatomical imaging, a rapid acquisition with relaxation enhancement (RARE) MRI sequence (TR/TE = 4000/23 ms; RARE factor, 4; number of averages, 2; FOV, 35.4 × 35.4 mm^2; image matrix, 128 × 128; slice thickness, 0.754 mm) was used to collect 40 contiguous images across the mouse torso, allowing tumor visualization.

For diffusion MRI, treatment and therapy monitoring began approximately 21 days post xenograft inoculation, when tumors reached the size of 300–800 mm^3. Tumor sizes were determined from region of interests (ROI) drawn from anatomical MRI images. On the day of treatment, mice were either injected with: a) 0.9% saline intravenously (i.v), b) 100mg/kg CPT-11 intraperitoneally (i.p.) or c) 5mg/kg CRLX101 (i.v.). Anatomical and diffusion MRI scans were acquired immediately before treatment (day 0, baseline), 2, 4 and 7 days posttreatment. A total of 19 mice were imaged for this study. Both CRLX101 and control groups contained 7 mice. Within those treatment groups, N = 3 were imaged on days 0, 2 and 4 and N = 4 were imaged on days 0, 2, 4 and 7. All mice in the

CPT-11 group (N = 5) were imaged on days 0, 2, 4 and 7.

Diffusion MRI was acquired with a spin-echo diffusion MRI sequence [69] (TR/TE = 3000/25 ms ; Δ = 15 ms, δ = 3 ms, with three b values = 0, 800, and 1,200 s/mm^2 acquired in 3 orthogonal directions; FOV, 35 × 25 mm^2; image matrix, 175 × 125 (zero filled to 256 × 125 ; slice thickness, 0.754 mm). The number of slices acquired in each study was determined by the tumor size to ensure full coverage of the tumor mass.

ADC tumor maps were generated using these trace diffusion images by fitting to the Stejskal-Tanner equation [68] using MATLAB. TheS_0 images derived from this analysis were used as templates to segment the tumor region. Segmentation was done manually using MRIcro (http://www.mricro.com).

4.4.3 Modeling Tumor Growth Using Diffusion MRI

A simplified logistic model of tumor growth, developed by Atuegwu *et al.* [230], was applied to the dynamic diffusion MRI data in order to estimate tumor cell proliferation rates and tumor cell numbers. Since it was not possible to spatially coregister tumor images from multiple time points on a voxel-by-voxel basis, we only considered ROIs based on the whole tumor. Briefly, the model is defined by

$$N(t) = \frac{\vartheta N(t_1)}{N(t_1) + (\vartheta - N(t_1))e^{-kt}}, \tag{4.1}$$

where $N(t)$ is the number of cells per tumor voxel at time t, $N(t_1)$ is the number of cells present at $t = t_1$, the first time point in the calculation. k is the cell proliferative rate and ϑ the cell carrying capacity in the population, here assumed to be the maximum number of cells in the imaging voxel. If a linear relationship between ADC and cellularity is assumed, ADC can be related to cell number by

$$\frac{ADC(t) - ADC_w}{ADC_{min} - ADC_w} = \left(\frac{N(t_1)}{\vartheta}\right), \tag{4.2}$$

and derive k and $N(t)$ by combining (4.1) and (4.2) [229]:

$$\frac{ADC(t) - ADC_w}{ADC_{min} - ADC_w} = \left(\frac{ADC(t_1) - ADC_{min}}{ADC(t_1) - ADC_w}\right) e^{-kt}. \tag{4.3}$$

$ADC_w$is the ADC of free water (~3 × 10^{-3} mm^2/s) [236] and ADC_{min} is the minimum voxel ADC value in a given tumor.

The ability of the model to calculate tumor growth was tested by calculating $N_{calculated}(4)$ and $N_{calculated}(7)$, which were calculated with k values derived from day 0/2 and day 2/4 ADC data respectively using equation 6. These were compared to $N_{estimated}(4)$ and $N_{estimated}(7)$, which were measured from actual ADC data taken on day 4 and 7 and calculated using equation 5.

The cellular proliferation rate k using a combination of ADC data from different time points (day 0/2, 0/4, 2/4, 4/7) were also calculated for each individual.

4.4.4 Histological Assessment

A separate group of animals with Daudi lymphoma tumors were prepared for histological comparison with noninvasive imaging (N = 24). Animals were divided into control, CPT-11 and CRLX101 groups. The animals were treated identically as those in the imaging studies. At days 0, 2, 4 and 7, animals (N = 2 per time point) from each treatment group were sacrificed by transcardiac perfusion and tumors were excised. Tumors were placed in 4% paraformaldehyde overnight, dehydrated in 70% ethanol and subsequently embedded in paraffin. Paraffin blocks were sectioned at a slice thickness of 4 μm.

Paraffin sections were deparaffinized in xylene and rehydrated through a descending gradient of alcohol (100%, 95%, 80%, 2 minutes at each concentration) and then water.

Antigen retrieval was achieved with 10mM Tris, 1mM EDTA, 0.05% Tween 20 pH9.0 for 20 minutes in a steamer and then cooled for 20 minutes. Individual sections from each treatment cohort and time point were then incubated with primary antibodies to the cellular proliferation marker Ki-67 (1:200, Neomarkers, RM-9106-SO) or the apoptotic marker cleaved caspase-3 (1:500, Invitrogen, 700182). Immunohistochemistry was performed on a DAKO Autostainer utilizing a peroxidase DAB method (Leica, Novalink RE7150-K) followed by counterstaining with hematoxylin.

Staining for apoptosis was performed using a terminal nucleotidyl transferase-mediated nick end labeling (TUNEL) assay (Roche, Insitu Cell Death Detection Kit) and visualized with a peroxidase DAB method (Leica, Novalink), followed by counterstaining with hematoxylin. Corresponding sections were also stained with H&E for overall tumor and cellular morphology.

All slides were scanned on a Ventana Coreo slide scanner for visualization.

4.4.5 Statistical Analysis

Comparison of ADC, tumor size and cell proliferation data among the three treatment groups was accomplished at each time point using a non-parametric Kruskal-Wallis test. Multiple comparison tests were performed with Bonferroni correction after a Mann-Whitney test. $N(t)$ data were compared using Pearson's (PCC) and concordance (CCC) correlation coefficients. A p-value of 0.05 or smaller was considered to be statistically significant.

4.5 Results

4.5.1 Diffusion MRI is Sensitive to Early CRLX101 Treatment Response

Diffusion MRI was used to quantify the temporal response of the lymphoma microenvironment to CRLX101, CPT-11, and control treatments in animals implanted with Daudi tumors. ADC maps of representative tumor response to the various treatment groups are shown in figure 4.1. According to figure 4.1, ADC values remain relatively constant for the control animal (top row) over the course of 7 days, with most of the tumor volume having relatively low ADC values (green) at each time point. A small pocket of high ADC can be seen by day 7, possibly due to spontaneous necrosis as a result of increasing tumor size. The CPT-11 treated animal (bottom row) showed a similar ADC map pattern throughout most of the tumor, with low ADC values over a substantial part of the tumor volume across all time points. On day 2 after CPT-11 administration, clusters of high ADC values (as indicated by red to orange pixels) can be seen around the edges of the tumor, suggesting CPT-11 response. By day 4 and day 7, small high ADC clusters still existed, but appeared to approximately the same as were seen on day 2. The ADC map patterning remained similar between day 4 and day 7. Compared to the two other treatment cohorts, the CRLX101 treated tumor (middle row) showed a steady increase in the ADC value throughout the whole tumor bulk. By day 2 posttreatment, the whole tumor volume showed an increase in ADC. This trend continued onto day 4 and day 7. These findings were also observed when visualized with one-dimensional histograms of ADC tumor voxel distributions (figure 4.2).

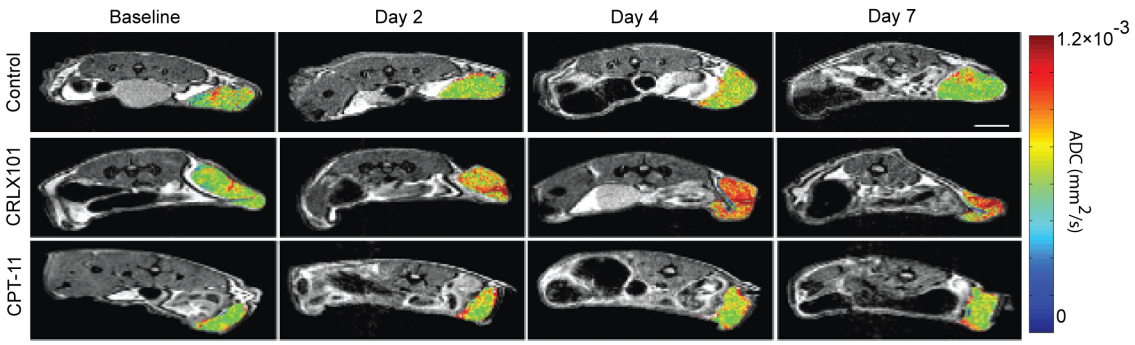

Figure 4.1: Diffusion MRI is sensitive to early CRLX101 response. Representative ADC map of Daudi tumors are shown as color overlays on T_2-weighted anatomic MRI images. diffusion MRI images were acquired on day 0 (pretreatment), day 2, day 4 and day 7 for control (top row), CRLX101 treated (middle row) and CPT-11 treated (bottom row). diffusion MRI clearly shows an increased ADC response to CRLX101 throughout the whole tumor mass as early as day 2 posttreatment, compared to CPT-11 treated and control animals (scale bar = 10 mm).

To compare the diffusion MRI response between treatment groups, the mean percentage change of ADC values from baseline were calculated and graphed in figure 4.3. CRLX101 treated tumors clearly exhibited increasing tumor ADC values over the course of 7 days compared to baseline (16 ± 9%, 24 ± 10% and 49 ± 17% change from baseline on day 2, 4 and 7, respectively). CPT-11 treated tumors also showed a mean increase in ADC values over the week (5 ± 5%, 14 ± 7% and 18 ± 6%), while control tumors showed a slight decrease in ADC value compared to baseline (-4 ± 3%, -7 ± 3% and -9 ± 3%). Compared to the control group, the increases observed in the CRLX101 group were significant on all days (day 2: $p = 0.02$, day 4: $p < 0.01$, day 7: $p < 0.01$). This was not the case for the CPT-11 group (day 2: $p = 0.4$, day 4: $p = 0.05$, day 7: $p = 0.05$).

4.5.2 Diffusion MRI Response Correlates with Traditional Measurements of Tumor Growth

Drug efficacy is typically measured by analyzing tumor volumetric changes over time. Tumor volume information was obtained from MRI scans concurrent with diffusion MRI studies. Volume changes as sorted by treatment cohort are shown in figure 4.4. Control tumors steadily increased in size during the week time course (25 ± 17%, 49 ± 15% and 130 ± 44% change from baseline on day 2, 4 and 7, respectively), while CRLX101 treated tumors steadily decreased in size (-5 ± 3%, -30 ± 4% and -45 ± 13%). As with the ADC values, size decrease in the CPT-11 treated group was less

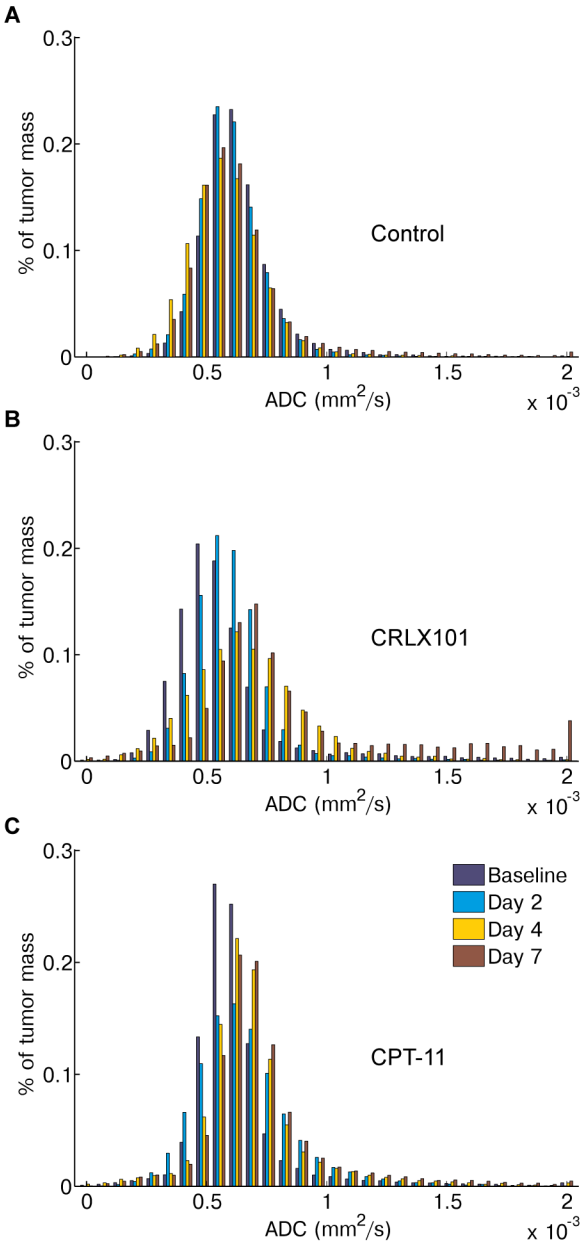

Figure 4.2: Histogram analysis of diffusion MRI. One dimensional histogram of ADC values from animals treated with (A) saline, (B) CRLX101 and (C) CPT-11 over the course of 1 week are shown. In a control animal (A), the distribution of ADC values within the tumor remained relatively stable over the course of the week. In a CRLX101 treated animal (B), a gradual right shift of the ADC value distribution toward higher values can be observed as early as day 2 and continuing onto day 4 and 7. In the CPT-11 treated animal, the ADC distribution showed a slight right shift toward higher values by day 4. However, the magnitude of this shift was less than that of observed in (B). The day 7 distribution remained similar to the day 4 histogram. These observations are consistent with the MR images (figure 4.1), and highlight the efficacy of CRLX101.

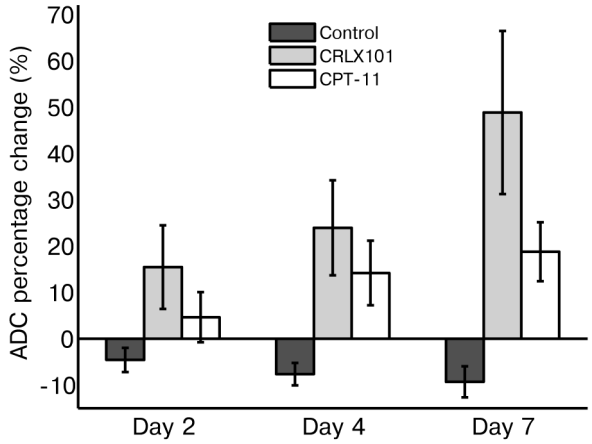

Figure 4.3: ADC changes over treatment week show efficacy of CRLX101. Percentage change of mean ADC values compared to baseline is graphed for the three different treatment groups over one week posttreatment. Plots show a significant increase in ADC for CRLX101 treated animals compared to CPT-11 and control (p <0.001). CPT-11 animals showed a slight increase (p >= 0.05) in the ADC values over the week compared to baseline, while control animals showed a slight decrease. CRLX101 treated animals showed an increase in ADC values at all time points, which was significant on day 2 (p = 0.02), day 4 ($p < 0.01$) and day 7 ($p < 0.01$). Error bars denote standard error.

drastic (-15 ± 5%, -22 ± 13% and -26 ± 8%) compared to the nanoparticle-treated group. The tumor size decreases in the CRLX101 treated group were not significantly different to control on day 2 (p = 0.08), but were significant by days 4 and 7 (both p <0.01). In comparison, CPT-11 group tumor size changes were only significantly different to the control group on day 4 (p <0.01).

4.5.3 Logistic Model of Tumor Growth can be Applied to Diffusion MRI of Malignant Lymphoma

Tumor cell number determined by incorporating diffusion MRI data into a model of tumor growth is shown in figure 4.5. $N_{calculated}$ compared to $N_{estimated}$for days 4 and 7 are shown in figures 4.5A and 4.5B respectively. The PCC between $N_{calculated}(4)$ and $N_{estimated}(4)$ is 0.92 (p <0.0001). The CCC is 0.83. PCC and CCC between $N_{calculated}(7)$ and $N_{estimated}(7)$ are 0.91 (p <0.0001) and 0.9. These values demonstrate a strong relationship between the simulated and estimated data, demonstrating that the logistic model is applicable to this lymphoma model.

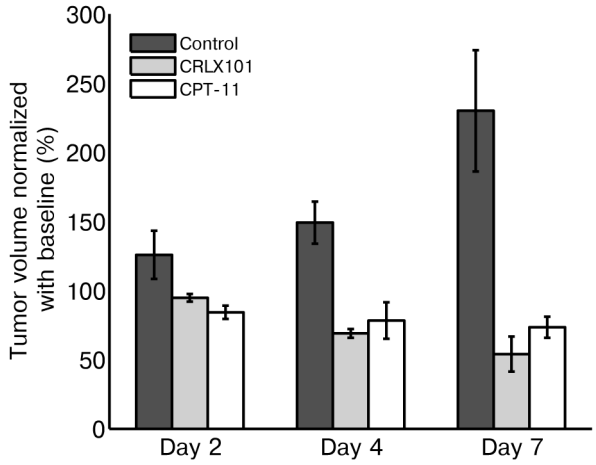

Figure 4.4: Tumor volume size changes over treatment week. Mean tumor sizes, as measured from anatomical MRI images, are graphed for the three different treatment groups over one week posttreatment. CRLX101 treated tumors decreased significantly compared to control tumors over 7 days (p <0.001) and significantly different to CPT-11 tumors on day 7 (p = 0.01). Compared to baseline, CRLX101 tumor sizes significantly decreased on both day 4 and 7 (p <0.01). Error bars denote standard error.

4.5.4 Modeling of Tumor Proliferation using Diffusion MRI show Antiproliferative Activity of CRLX101

Model-derived mean cell proliferation rates (in units of 1/day) measured from different time points across treatment groups are shown in figure 4.6. Corresponding boxplots are shown in figure 4.7. CRLX101 treated animals showed negative tumor proliferation rates across all time points (-0.09 ± 0.05, -0.05 ± 0.03, -0.05 ± 0.01 and -0.11 ± 0.05 for day 0/2, 0/4, 2/4 and 4/7 respectively) and were significantly different (p =0.02) to control tumors (0.03 ± 0.02, 0.02 ± 0.01, 0.02 ± 0.02 and 0.04 ± 0.04). CPT-11 animals (-0.04 ± 0.04, -0.02 ± 0.02, -0.06 ± 0.02 and 0.01 ± 0.01) showed negative proliferation rates between day 0 and day 4. These were significantly different to controls for rates calculated between day 2/4 (p = 0.03). Interestingly, proliferative rates in CPT-11 tumors calculated between day 4 and 7 became positive.

4.5.5 Histological Assessment of CRLX101 Response

Treatment-induced changes observed by diffusion MRI were correlated with histological observations of tumor response. Tumor sections were stained for activated (cleaved) caspase-3 to moni-

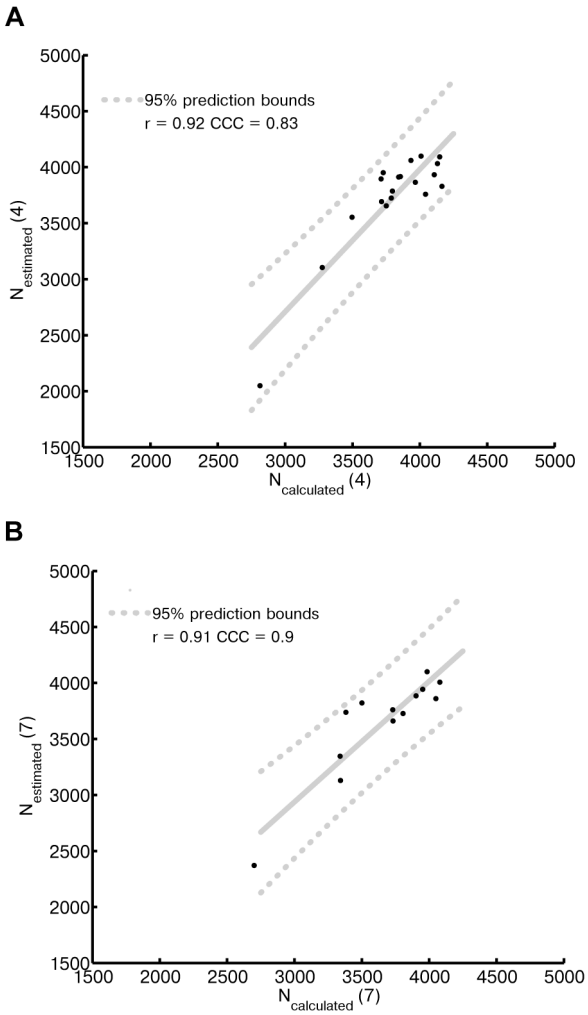

Figure 4.5: A logistic model of tumor growth can be applied to ADC data. (A) $N_{calculated}(4)$ (using ADC data from day 0 and day 2) is compared to $N_{estimated}(4)$. The linear fit (with 95% prediction intervals) is also plotted. The Pearson's correlation coefficient, r, is 0.92 (p = 0.0001) and the concordance correlation coefficient, CCC, is 0.83. (B) $N_{calculated}(7)$ (using ADC data from day 2 and day 4) is compared to $N_{estimated}(7)$. r = 0.91 (p = 0.0001) and CCC = 0.9.

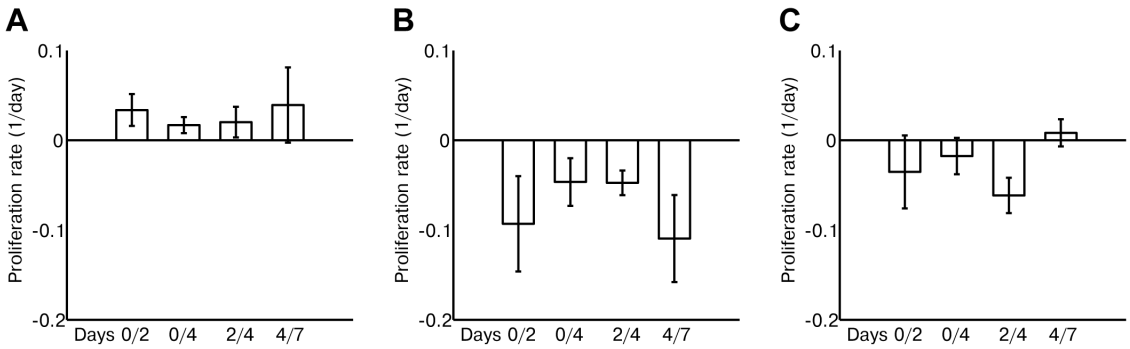

Figure 4.6: Cellular proliferation rates for different treatment groups were calculated by applying ADC data to a logistic model of tumor growth. Rates were calculated for (A) control, (B) CRLX101 and (C) CPT-11 animals between day 0/2, day 0/4, day 2/4, and day 4/7. Rates from CRLX101 animals were negative for all time periods and were significantly different to controls (p = 0.02). Rates for CPT-11 animals were negative between day 0 to day 4, being significantly different to controls between day 2/4 (p = 0.03). By day 4/7, CPT-11 proliferation rates became positive and similar to controls. Error bars denote standard error.

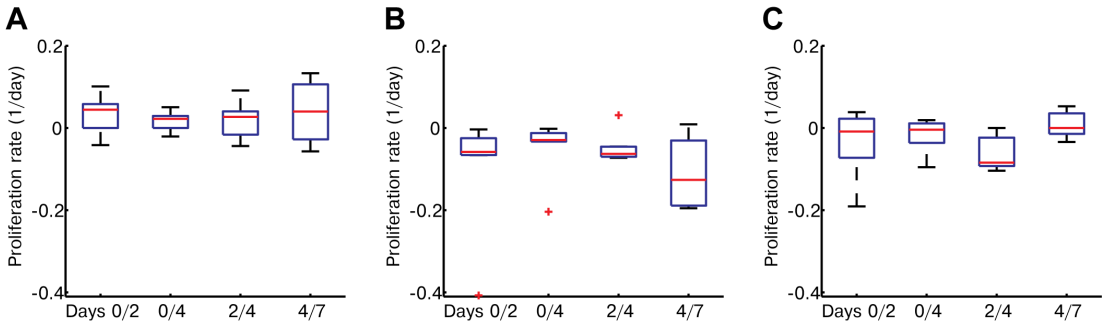

Figure 4.7: Boxplots of cellular proliferation rates for different treatment groups calculated by applying ADC data to a logistic model of tumor growth. Boxplots for (A) control, (B) CRLX101 and (C) CPT-11 animals between day 0/2, day 0/4, day 2/4, and day 4/7 are shown.

tor apoptotic activity (figure 4.8A). Control tumors showed minimal staining for active caspase-3 throughout the week. In comparison, CRLX101 treated tumors showed a dramatic increase in caspase-3 activation on day 2. Levels remained increased compared to time-matched control tumors on day 4 and day 7, albeit lower than day 2 cleaved caspase-3 levels. CPT-11 treated animals also showed a noticeable increase in active caspase-3 levels compared to control tumors on day 2. CPT-11 active caspase-3 levels were indistinguishable to time matched controls by day 4 and day 7. Analysis using a TUNEL assay (figure 4.8B) to stain for apoptotic cells by detecting 3´ DNA strand breaks (a biochemical hallmark of apoptosis) showed similar results. CRLX101 treated tumors showed an increase in apoptotic cells by day 2 of treatment, which persisted on day 4 and day 7. CPT-11 treated tumors did not show a noticeable increase in apoptic cells on day 2 post-treatment, but a number of apopotic cells were observed on day 4 and day 7. By comparison, control tumors did not show an increase in apoptotic cell staining throughout the week.

Since the active ingredient of CRLX101 and CPT-11, camptothecin, inhibits cellular proliferation, we also stained tumors using the cellular proliferation marker Ki-67 (figure 4.8C). Control tumors maintained high Ki-67 expression throughout the week. By comparison, both CRLX101 and CPT-11 treated tumors showed decreased Ki-67 staining by day 2 of treatment. Ki-67 expression in CRLX101 tumors decreased steadily throughout the week, while Ki-67 expression in CPT-11 treated tumors on day 4 remained similar to day 2 and were comparable to baseline by day 7.

H&E-stained sections from the control group showed a dense cellular pattern that remained consistent from baseline to day 7 (figure 4.8D). By comparison, CRLX101 tumors showed a gradual decrease in cellular density over 7 days. An increase in the number of amorphous cells can be observed in day 4 and day 7 tumors. CPT-11 tumor sections show a slight decrease in cellular density on day 2. By day 4 and day 7, the cellular patterns have reverted to baseline patterning. These cell density pattern differences between treatment groups were also seen on the other hematoxylin-stained sections (figure 4.8A–C).

4.6 Discussion

In the current study, diffusion MRI was used to follow the response of a preclinical model of malignant lymphoma to a targeted nanotherapy (CRLX101) and its small molecule chemotherapy coun-

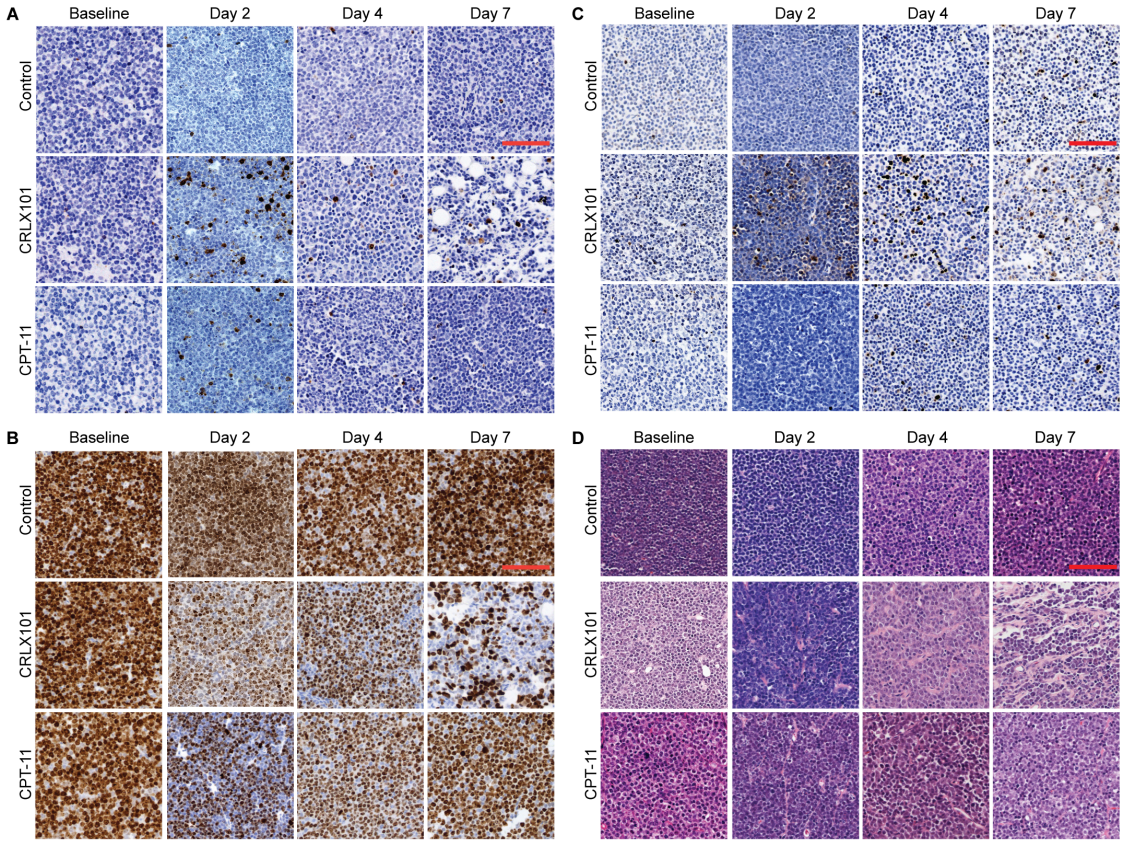

Figure 4.8: Histological assessment of CRLX101 and CPT-11 response. Tumors treated with CRLX101 (5 mg/kg), CPT-11 (100 mg/kg) or saline were harvested for histology on days 0, 2, 4, and 7. Tumor samples were subsequently sectioned and stained with (A) Cleaved caspase-3 (costained with hematoxylin), (B) TUNEL (costained with hematoxylin), (C) Ki-67 (costained with hematoxylin) and (D) H&E (scale bar = 500 µm).

terpart (CPT-11). As shown in figures 4.1 and 4.3, CRLX101 treatment led to quantifiable changes in ADC as early as day 2. By comparison, CPT-11 treatment also resulted in detectable changes in ADC, but was attenuated compared to the CRLX101 treatment. This correlated with tumor growth kinetics, which indicated that CRLX101 treatment resulted in marked tumor regression while only mild regression was seen with CPT-11 treatment (figure 4.4). Moreover, diffusion MRI results correlated with histology. CRLX101 and CPT-11 treated tumors showed increased apoptotic events by day 2. Decreased cellularity was observed in both treatment cohorts compared to controls across the week. A decrease in the proliferation marker Ki-67 was also observed in both treatment cohorts. This reflects the fact that CPT inhibits cell proliferation and is concordant with previous studies showing high topoisomerase I inhibition by CRLX101 and CPT-11 within 48 hours of administration [217]. Taken together, these results confirm the improved efficacy of CRLX101 compared to small molecule chemotherapy. Furthermore, diffusion MRI was able to demonstrate this improved efficacy at an early time point.

Other functional imaging techniques are being investigated to monitor early responses in lymphoma [221]. Many of these studies involve nuclear imaging, specifically PET. In particular, ^{18}F-fluoro-2-deoxy-d-glucose (FDG-PET) [13, 237, 238] and 3'-^{18}F-fluoro-3'-deoxy-L-thymidine [239, 240, 107] are promising imaging biomarkers of lymphoma response. Interpretation of nuclear imaging studies can be complex, as many different physiological processes can result in a positive signal during treatment. For example, local inflammation following therapy can increase the FDG-PET signal, masking treatment response [241]. Diffusion MRI readouts are less sensitive to such inflammatory effects [192]. Concerns of ionizing radiation overexposure, especially in lymphoma patients who may be exposed to serial imaging scans and/or radiation therapy [242] also necessarily limits the number of nuclear imaging scans that can be obtained from a patient, especially at early treatment time points.

Although ADC by itself is already a promising imaging biomarker to indicate tumor response to CRLX101, the availability of ADC datasets from multiple time points enables mathematical modeling of tumor growth. This potentially allows the prediction of future treatment response in an individual patient. We applied a simple logistic model of tumor growth [229] to ADC data. The model makes the simplifying assumption that each imaging voxel consist only of tumor cells and

that ADC changes are entirely due to the reduction in cellularity; yet it still provides instructive predictions using diffusion MRI datasets. This was shown by the strong correlation between simulated (using data from previous time points) and estimated (data from the time point of interest) tumor cell number at both day 4 and day 7 (figure 4.5). Proliferation rates generated from this model separated CRLX101-treated and control groups (figure 4.6) and highlighted the enhanced antiproliferative effect of CRLX101 [217]. Analysis of proliferative rates across time points may add insights to a treatment's mode of action. For example, consideration of the CPT-11 ADC and tumor growth data alone through day 7 would indicate that the tumor may still be responding to treatment, albeit less than with the nanotherapy. However, analysis of the proliferation data indicated that between day 4 and 7 CPT-11 tumors showed a trend toward positive proliferation rates, suggesting treatment failure. The latter analysis is consistent with histology; by day 7 the Ki-67 staining in CPT-11 tumors were similar to baseline and control. In contrast, CRLX101 proliferation rates were negative between day 0 and day 2, increased slightly between days 2 and 4 before decreasing again from day 4 to 7. This observation is consistent with CRLX101 Ki-67 staining, but is not immediately apparent from looking at ADC changes alone. The reason for this fluctuation of proliferation rate is unclear; tumor uptake and biochemical activity of CRLX101 have only been followed for up to 48 hours [217]. It has been suggested that CRLX101 may have antiangiogenic effects and enable prolonged drug release via hydrolytic and enzymatic cleavage of the cyclodextrin-polymer [19]. Such effects may be synergistic and lead to the increased efficacy observed at later time points. Techniques that can probe CRLX101's dynamic antiangiogenic effects within the tumor, such as dynamic contrast-enhanced MRI [131], may be able to elucidate this process.

Since it was difficult to spatially coregister individual tumor images across time points, imaging data were only analyzed at a whole-tumor ROI level. Thus, the heterogeneity of the tumor mass, which may also be an important determinant to treatment response, was neglected. This may be addressed in future studies by prudent spatial coregistration across time points. Furthermore, the current model can be integrated into more sophisticated models [208] of tumor growth by incorporating data acquired concurrently with other modalities (e.g.PET) [201].

In conclusion, we have demonstrated that diffusion MRI can monitor the early response to CRLX101 treatment in a preclinical model of malignant lymphoma. Modeling of the ADC data

emphasized the enhanced antiproliferative effect of CRLX101 compared to controls and CPT-11. This demonstrates the utility of diffusion MRI for preclinical and clinical evaluation of targeted nanotherapies such as CRLX101 and suggests that an image-driven modeling approach can provide insights to their mechanism(s) of action *in vivo*.